The wake structure behind a porous obstruction and its implications for deposition near a finite patch of emergent vegetation

The wake structure behind a porous obstruction and its implications for deposition near a finite patch of emergent vegetation

Zhengbing Chen,[1,2] Alejandra Ortiz,[2] Lijun Zong,[2] and Heidi Nepf [2]

[1]   This experimental study describes the mean and turbulent flow structure in the wake of a circular array of cylinders, which is a model for a patch of emergent vegetation. The patch diameter, D, and patch density, a (frontal area per volume), are varied. The flow structure is linked to a nondimensional flow blockage parameter, $C_D a D$, which is the ratio of the patch diameter and a drag length scale $(C_D a)^{-1}$. C_D is the cylinder drag coefficient. The velocity exiting the patch, U_e, is reduced relative to the upstream velocity, U_∞, and U_e/U_∞ decreases as flow blockage ($C_D a D$) increases. A predictive model is developed for U_e/U_∞. The wake behind the patch contains two peaks in turbulence intensity. The first peak occurs directly behind the patch and is related to turbulence production within the patch at the scale of individual cylinders. The second peak in turbulence intensity occurs at distance L_w downstream from the patch and is related to the wake-scale vortices of the von Karman vortex street. The presence of the flow U_e in the wake delays the formation of the von Karman vortex street until distance L_1 $(<L_w)$ behind the patch. Both L_1 and L_w increase as U_e increases and thus as the flow blockage ($C_D a D$) decreases. L_1 sets the distance behind the patch within which fine-particle deposition can occur. Beyond L_w, turbulence associated with the wake-scale vortices inhibits deposition.

1. Introduction

[2] Flow through a porous obstruction occurs in many engineering and science contexts, including pile groups, heat exchangers, and aquatic and terrestrial vegetation. The motivation for this project is the study of aquatic vegetation. Because it reduces the near-bed velocity and stabilizes soil substrate, vegetation is regarded as a protection for shorelines and riverbanks [*Micheli and Kirchner*, 2002; *Gedan et al.*, 2011]. In addition, vegetation improves water quality by removing nutrients and releasing oxygen to the water column [*Wilcock et al.*, 1999; *Schulz et al.*, 2003], and it provides important habitat [*Kemp et al.*, 2000]. In recognition of its positive ecological function, efforts to restore vegetation have increased.

[3] Until recently, most research on vegetation hydrodynamics has considered meadows of uniform horizontal distribution. However, vegetation is also found in patches of finite length and width. The diversion of flow around a patch of finite width can produce locally enhanced flow that promotes

erosion at the patch edge, which may inhibit the lateral expansion of the patch [*Fonseca et al.*, 1983; *Temmerman et al.*, 2007; *Bennett et al.*, 2008, *Bouma et al.*, 2009; *Rominger and Nepf*, 2011]. This hydrodynamic control on patch expansion represents a feedback between vegetation and geomorphology that may set limits on the potential for vegetation restoration in channels and coastal zones. *Vandenbruwaene et al.* [2011] note that in the initial stage of growth, vegetation often appears in circular patches. In channels, these patches subsequently grow predominantly in the downstream direction [*Sand-Jensen and Madsen*, 1992]. This suggests that the wake of the patch creates conditions for deposition that favor patch expansion in this direction. However, the flow adjustment near a finite patch and resulting deposition is not completely understood. Our paper provides new observations of flow adjustment and deposition near a circular patch of model emergent vegetation.

[4] Recent studies have described the wake behind a circular array of circular cylinders [*Takemura and Tanaka*, 2007; *Nicolle and Eames*, 2011; *Zong and Nepf*, 2012]. Because the array is porous, some flow passes through it, and the presence of this bleed flow delays the onset of the von Karman vortex street, relative to what is observed behind a solid obstruction. A steady wake exists behind the patch, within which the velocity, U_1, remains constant over length scale L_1 (Figure 1). The steady wake velocity U_1 is somewhat lower than the velocity exiting the patch, U_e, because flow adjustment continues slightly beyond the patch. The steady wake and delayed onset of the von

[1]Department of Hydraulic Engineering, Tsinghua University, Beijing, China.
[2]Department of Civil and Environmental Engineering, Massachusetts Institute of Technology, Cambridge, Massachusetts, USA.

Corresponding author: H. Nepf, Department of Civil and Environmental Engineering, Massachusetts Institute of Technology, Room 48-216D, 77 Massachusetts Ave., Cambridge, MA 02139, USA. (hmnepf@mit.edu)
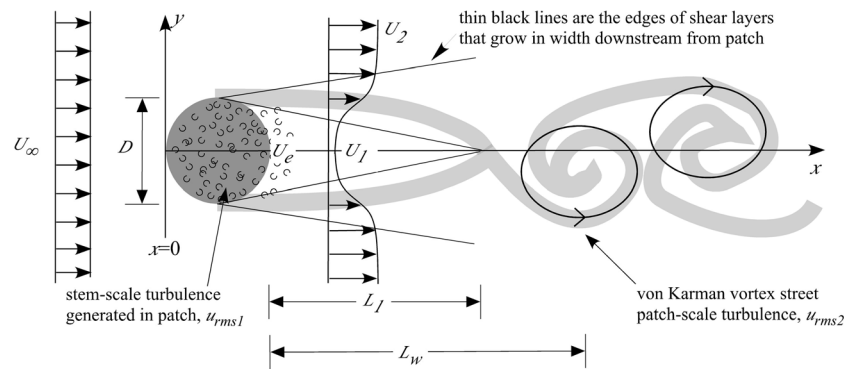
Figure 1. Top view of a circular patch of emergent vegetation, shown by dark gray circle of diameter D. Injections of dye at the outer edges of patch (thick gray lines) reveal the evolution of the wake. Velocity exiting the patch ($U_e = u(x = D)$) is diminished relative to upstream velocity (U_∞). The velocity decreases further to the steady wake region (U_1). The flow within the wake delays the onset of the von Karman vortex street to the end of the steady wake, $x = L_1 + D$. The wake contains two scales of turbulence: stem-scale turbulence (shown with small thin semicircles), which peaks within the patch, and patch-scale turbulence (black circles with arrows), which peaks at $x = L_w + D$.

Karman vortex street have been visualized by *Zong and Nepf* [2012] using traces of dye injected at the outer edges of the patch. This is shown schematically in Figure 1, with the dye trace shown as a thick gray line. Because the steady wake is fed only by water entering from upstream through the patch, there is no dye in this region, i.e., the steady wake appears as a clear region directly behind the patch, in between the two dye streaks. After distance L_1, the dye streaks come together and a single, patch-scale, von Karman vortex street forms. At this point the velocity at the wake centerline begins to increase. It is interesting to note that bed friction may also suppress the formation of von Karman vortices. *Chen and Jirka* [1995] studied shallow conditions, characterized by the stability parameter $S = c_f D/h$. Here, c_f is the bottom friction coefficient, D is the transverse body dimension, and h is the water depth. If the stability parameter is greater than a critical value, S_c, bed friction may suppress the vortex street. For a solid obstructions, $S_c = 0.2$, and for a porous plate ($\phi = 0.5$), $S_c = 0.09$. In our study, the maximum value of S is 0.019, much less than S_c for either porous or solid obstructions. Therefore, bed friction is not contributing to the suppression of vortex formation observed in our study, although it may be important in some field conditions.

[5] The patch wake contains two peaks in turbulence intensity. The first peak occurs directly behind the patch and is related to turbulence production within the patch at the scale of individual stems. The second peak, located L_w from the back of the patch, is related to the generation of the von Karman vortex street. L_w is called the wake formation length, a name taken from previous studies on solid body wakes [*Williamson*, 1996]. *Takemura* and *Tanaka* [2007] also noted these two distinct scales of turbulence in the wakes of circular groupings of cylinders.

[6] We expect that deposition near a patch of vegetation will be influenced by the spatial distribution of velocity and turbulence in the patch and wake. To this end, it would be useful to predict the exit velocity U_e, from which one could estimate the velocity and turbulence intensity within the patch. We also want to describe the distances to the onset of the von Karman vortex street (L_1) and the second turbulence peak (L_w). In this paper we develop predictive models for

these parameters as a function of patch geometry and stem density. The link between these parameters and the deposition pattern around a circular patch of emergent cylinders (stems) is also explored.

2. Methods

[7] Experiments were conducted in a 16 m long recirculating flume with a test section that is 1.2 m wide and 13 m long. The bed of the flume is horizontal. The circular patches have diameters, D, between 5 cm and 42 cm and are constructed from wooden circular cylinders with diameter $d = 0.64$ cm. The cylinders are fitted into a baseboard with a staggered array of holes. The stem density is described by n, the number of cylinders per bed area, and the frontal area per volume, $a = nd$. The solid volume fraction is $\phi = \pi ad/4$. We consider 19 patch configurations, given in Table 1. In every case the cylinders are emergent, i.e., occupy the entire flow depth, $h = 13.3 \pm 0.2$ cm. The mean upstream velocity U_∞ is 9.8 ± 0.5 cm s^{-1}. As noted above, none of the cases fall into the shallow flow regime of *Chen and Jirka* [1995].

[8] The streamwise coordinate is x, with $x = 0$ at the leading edge of the patch (Figure 1). The lateral coordinate is y, with $y = 0$ at the centerline. The vertical coordinate is z. The three components of velocity, (u, v, w), are measured along the centerline of the patch using a Nortek Vectrino. This longitudinal transect begins 1 m upstream of the patch and extends 5 to 9 m downstream of the patch. At each position the velocity is recorded at middepth for 240 s at a sampling rate of 25 Hz. Based on previous studies in the same flume [*White and Nepf*, 2007], the velocity measured at middepth is a good approximation (within 5%) of the depth average. Each velocity record is decomposed into time averages ($\bar{u}$, $\bar{v}$, $\bar{w}$) and fluctuating components (u', v', w'). The turbulence intensity is described by the root-mean-square of the fluctuating components, (u_{rms}, v_{rms}, w_{rms}).

[9] The length scale L_1 is estimated from the longitudinal velocity transect as the distance from the downstream edge of patch ($x = D$) to the last point before the velocity begins to increase, signaling the beginning of wake-scale mixing associated with the von Karman vortex street (Figure 2).

Table 1. Summary of Parameters[a]

Case	Symbol	D (cm)	a (m⁻¹)	aD	C_D	C_DaD	ϕ (%)	U_e (cm s⁻¹)	U_1 (cm s⁻¹)	u_{rms1} (cm s⁻¹)	u_{rms2} (cm s⁻¹)	TKE$^{1/2}$ (cm s⁻¹)	L_w (cm)	L_1 (cm)	Re
1	solid diamond	10	25	2.5	2.1	5.3	13	3.2 (6.0, 2.6)	2.3	1.2	1.6	1.7	80 (10)	40 (5)	N
2	solid square	10	30	3.0	2.3	6.9	15	3.0 (3.0, 2.6)	0.9	1.7	2.2	2.5	65 (5)	35 (5)	N
3	solid triangle	10	47	4.7	3.0	14	24	3.6 (5.7, 3.4)	0.7	1.5	2.3	2.7	60 (5)	30 (5)	N
4	solid inverted triangle	10	86	8.6	4.0	34	43	1.4 (3.8, 1.1)	-	-	2.7	3.8	20 (5)	-	Y
5	solid left pointing triangle	12	5.7	0.7	1.2	0.8	2.8	6.7 (8.1, 5.2)	-	2.7	-	-	-	-	N
6	solid right pointing triangle	12	7.9	0.9	1.2	1.1	4.0	7.0 (7.2, 6.1)	5.6	2.0	0.9	1.0	200 (50)	80 (5)	N
7	solid five-point star	12	11	1.3	1.3	1.7	5.4	8.3 (8.3, 6.0)	5.0	2.3	0.9	0.9	150 (20)	90 (10)	N
8	solid circle	12	22	2.6	1.7	4.4	11	1.4 (7.3, 0.9)	0.7	1.2	2.0	2.2	80 (5)	40 (5)	N
9	solid six-point star	20	23	4.6	1.7	7.8	12	2.4 (5.4, 2.3)	0.6	1.0	3.1	2.2	100 (10)	60 (5)	Y
10	open diamond	22	31	6.8	2.4	16	16	0.4 (2.9, 0.0)	0.3	0.6	2.6	3.2	100 (5)	70 (5)	N
11	open square	22	5.6	1.2	1.2	1.5	2.8	6.9 (7.1, 5.7)	5.4	1.2	1.0	1.0	380 (50)	130 (20)	N
12	open triangle	22	5.9	1.3	1.2	1.6	3.0	6.6 (8.3, 6.5)	5.8	1.9	1.0	1.1	340 (40)	180 (10)	N
13	open inverted triangle	22	82	18	4.0	72	41	1.2 (1.6, 0.0)	-	-	3.2	4.9	30 (5)	-	Y
14	open left pointing triangle	22	11	2.3	1.3	3.0	5.3	5.5 (6.2, 5.4)	3.8	1.4	1.5	1.6	230 (20)	100 (10)	N
15	open right pointing triangle	22	22	4.8	1.7	8.1	11	1.9 (3.3, 1.9)	0.3	0.8	2.6	2.9	110 (10)	65 (5)	Y
16	open five-point star	42	6.1	2.6	1.3	3.3	3.1	6.2 (6.2, 4.5)	5.0	1.4	1.4	1.3	510 (100)	260 (20)	N
17	open circle	42	22	9.0	1.8	16	11	1.8 (1.9, 0.1)	0.5	0.6	3.0	4.0	160 (10)	100 (10)	Y
18	open six-point star	5.0	39	2.0	2.6	5.1	20	4.8 (7.2, 4.2)	0.7	2.8	1.8	1.9	35 (5)	14 (2)	N
19	cross	5.0	101	5.1	4.5	23	51	1.9 (2.8, 0.2)	-	-	3.0	3.5	17 (1)	-	Y

[a]Numbers in the parentheses are the uncertainty. For U_e the upper and lower limit is given in parentheses. For the lowest flow blockage ($C_DaD = 0.8$), no von Karman vortex street is formed, and U_1, L_1 and L_w are not relevant. For the three largest flow blockage ($C_DaD = 23, 34, 72$), wake structure is similar to bluff body, with no steady wake, and therefore U_1 and L_1 are not relevant. Re indicates whether there is (Y) or is not (N) a recirculation zone behind the patch. Instrument noise (0.3 cm s⁻¹) sets the lower limit at which u_{rms} can be resolved. The depth-averaged upstream velocity (U_∞) is 9.8 ± 0.5 cm s⁻¹, and flow depth h is 13.3 ± 0.2 cm. The cylinder density per bed area $n = a/d$, with $d = 6.4 \times 10^{-3}$ m in all cases.

The uncertainty of L_1 is based on the measurement spacing at that point (Table 1). The steady wake velocity (U_1) is measured in the region of constant velocity (e.g., see Figure 2). The exit velocity, $U_e = \bar{u}(x = D, y = 0)$ is the centerline velocity at the downstream edge of patch. Due to the dowel arrangement, it is not always possible to obtain a measurement exactly at this point, so that U_e is estimated by linear interpolation between the nearest measurement point upstream and downstream of $x = D$. An upper and lower limit for U_e are then estimated by linear extrapolation through two points upstream and then two points downstream of $x = D$. The estimate of U_e is included in Table 1, with upper and lower limits given in brackets. Finally, L_w is defined as the distance from the downstream edge of the patch to the second peak in u_{rms}, denoted u_{rms2}.

[10] Deposition was measured for two cases chosen to represent low- and high-flow blockage conditions (defined in section 3), respectively, case 16 ($D = 42$ cm, $a = 6.1$ m⁻¹, $C_DaD = 3.3$) and case 17 ($D = 42$ cm, $a = 22$ m⁻¹, $C_DaD = 16$). These are compared to a control experiment with no patch, but the same flow conditions. The suspended material consisted of 12-μ m-diameter spherical glass beads with a density of 2.5 g/cm³ and a settling velocity of 0.01 cm s⁻¹ (Potters Industry, Inc., Valley Forge, Pennsylvania). To measure deposition, numbered microscope slides (2.5 × 7.5 cm) were placed every 10 cm along the centerline from 1 m before the start of the patch to 6 m after the patch. Five smaller slides (2.5 × 2.5 cm) were placed within the patch by removing a single dowel at each position. This changed the stem density by 1%; e.g., in case 17, the change from 479 to 474 total stems changed a from 22.1 to 21.9 m⁻¹. The same slide configuration was used in the control experiment with no patch. The slides were weighed before placement. To prevent clumping, 650 g of sediment was mixed vigorously in several containers of water, after which the slurry was introduced at the upstream end of the flume. The sediment was mixed over depth and width in the flume within 1 min. After 4 h, the pump was slowly stopped

to prevent waves, and then the flume was slowly drained. The slides were left to dry in the flume for at least 2 days. Once dry, the slides were carefully removed from the flume and placed in an oven at 50°C for 2–3 h to ensure the removal of all excess moisture. Afterward, the slides were reweighed and the net deposition was calculated by differencing the weight of each slide before and after the experiment. The experiment was repeated three times, and the standard deviation among the three replicates used as an indication of uncertainty.

3. Adjustment of Mean Velocity to Patch

[11] In this section we consider how the mean velocity adjusts near the patch and develop predictive models for the
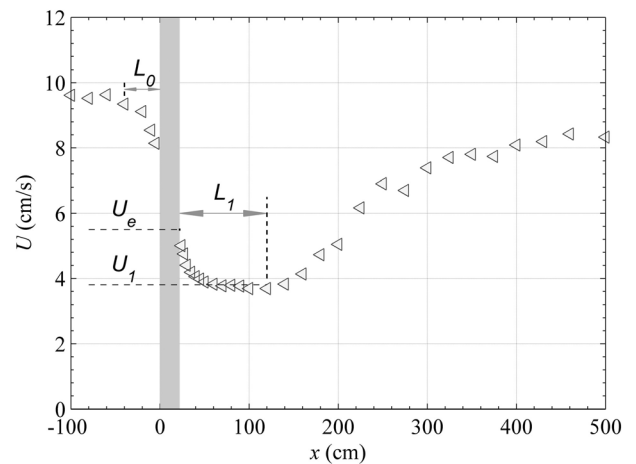

Figure 2. Streamwise velocity along the patch centerline ($y = 0$) for case 14 ($D = 22$ cm, $a = 0.11$ cm⁻¹, ϕ is 5.3%). Patch location is shown by gray bar. L_0 is the upstream adjustment length. The velocity exiting the patch is U_e. The steady wake velocity (U_1) is roughly constant until distance L_1 behind the patch.
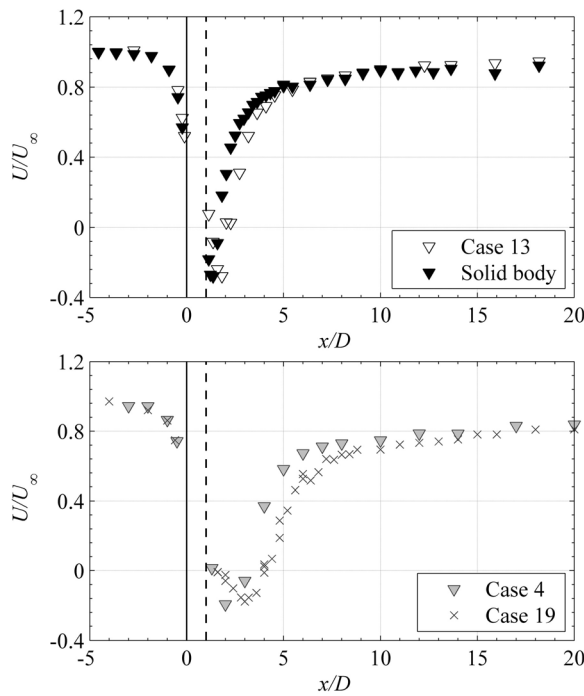
Figure 3. Longitudinal profiles of streamwise velocity. (top) For the highest flow blockage (case 13, $D = 22$ cm, $\phi = 0.41$ $C_D a D = 72$) the wake structure is nearly identical to that of a solid body of the same diameter ($D = 22$ cm). (bottom) Cases 4 ($D = 10$ cm, $\phi = 0.43$, $C_D a D = 34$) and 19 ($D = 5$ cm, $\phi = 0.51$, $C_D a D = 23$) also exhibit wake structure similar to a solid body. There is no steady wake region, and a recirculation zone occurs directly behind the patch. In each case the patch exists between $x/D = 0$ (solid vertical line) and 1 (dashed vertical line).

exit velocity (U_e), the steady wake velocity (U_1), and the length scale L_1. The basic evolution of the velocity field along the patch centerline is demonstrated with case 14 (Figure 2). Flow begins to decelerate at a distance L_0 upstream of the patch leading edge, and L_0 scales on D, similar to bluff bodies. The flow decelerates rapidly within the patch. Because the velocity continues to decelerate and diverge for a short distance after the patch, the exit velocity (U_e) is slightly larger than the steady wake velocity (U_1). The velocity U_1 is roughly uniform over the distance L_1, defined as the steady wake (Figure 2). Although not observed in our study, if the steady wake velocity is sufficiently small, specifically, $U_1 h/\nu < 500$, this region of the wake may become laminar. At distance L_1 from the patch the velocity begins to increase with distance, reflecting the start of the von Karman vortex street that provides a lateral flux of momentum into the wake.

[12] In a few cases solid volume fraction was sufficiently high that no steady wake region was observed (Figure 3). For example, the velocity transect for case 13 ($\phi = 0.41$, $D = 22$ cm) is nearly identical to a solid body with the same diameter, showing only a small shift in the position of the recirculation zone (Figure 3, top). Cases 4 ($\phi = 0.43$, $D = 10$ cm) and 19 ($\phi = 0.51$, $D = 5$ cm) are in transition toward a solid body wake. These wakes do not have a steady wake region, but the recirculation zone is elongated relative

to the wake of a solid body. The steady wake region was also absent for one of the sparsest patches (case 5, $\phi = 0.028$, $D = 12$ cm), which did not produce patch-scale van Karman vortices, although individual von Karman vortex streets occurred behind each cylinder within the patch. This condition of cylinders within the patch, i.e., uncoupled, individual wakes, was also observed at low solid volume fraction by *Takemura and Tanaka* [2007] and *Nicolle and Eames* [2011]. The transitions at both high and low solid volume fraction are discussed further in section 4.

3.1. Predictive Model for Patch Exit Velocity (U_e)

[13] Several researchers have studied the adjustment of flow to long, rectangular patches of vegetation. They defined two length scales that impact this adjustment. The first is the patch half width, b. The second is the canopy drag length scale, $L_c = 2(1 - \phi)/C_D a$, introduced by *Belcher et al.* [2003]. The drag coefficient, C_D, can be affected by the stem density, the stem Reynolds number, and the morphology of the individual canopy elements [*Tanino and Nepf*, 2008; *Nepf*, 2012a]. In this study we estimate C_D from Figure 5 of *Tanino and Nepf* [2008], based on ϕ and the stem Reynolds number within the patch, $Re_d = u_p d/\nu$, with u_p the average velocity within the patch. The ratio of patch half width to drag length scale creates the nondimensional flow blockage, $C_D a b$, which describes the flow adjustment to a long, rectangular patch of finite width $2b$ [*Rominger and Nepf*, 2011]. We adapt this parameter to a circular patch of diameter D, by defining the flow blockage as $C_D a D$, and recognizing that $D = 2b$. Drawing on the momentum balance described in *Rominger and Nepf* [2011], we expect the spatial scale of flow adjustment near a circular patch to be the maximum of the drag length scale and the patch half width ($D/2$). The following adjustment length, L, captures this maximum. Unlike *Rominger and Nepf* [2011], we retain the porosity ($1 - \phi$) for generality.

$$L = \left[\left(\frac{2(1 - \phi)}{C_D a} \right)^2 + \left(\frac{D}{2} \right)^2 \right]^{1/2} \qquad (1)$$

From (1) we anticipate two classes of flow behavior. For high-flow blockage, $C_D a D \gg 4$, the adjustment length reduces to the patch half width, $L = D/2$. For low-flow blockage, $C_D a D \ll 4$, the adjustment length reduces to the drag length scale, i.e., $L = L_c$. Note that at low-flow blockage, for which ϕ is typically $\ll 1$, we can approximate $L = 2(C_D a)^{-1}$ for this limit.

[14] The observations support that L is the appropriate scale parameter for flow adjustment near a circular patch of vegetation. When the longitudinal distance (x) is normalized by L, the rapid deceleration of flow within the patch collapses to a single linear relationship for all patch sizes and patch stem densities (Figure 4). From the data, we can estimate the mean slope of the nondimensional deceleration (dashed line in Figure 4).

$$A = d(u/U_\infty)/d(x/L) = 0.38 \pm 0.04 \qquad (2)$$

Based on the observations in Figure 4, we propose the following generalization for flow adjusting to a circular patch (Figure 5): The flow begins to decelerate at a distance $L_0 \sim D$ upstream of the patch, such that the velocity at the leading edge of the patch, U_0, is already diminished from the
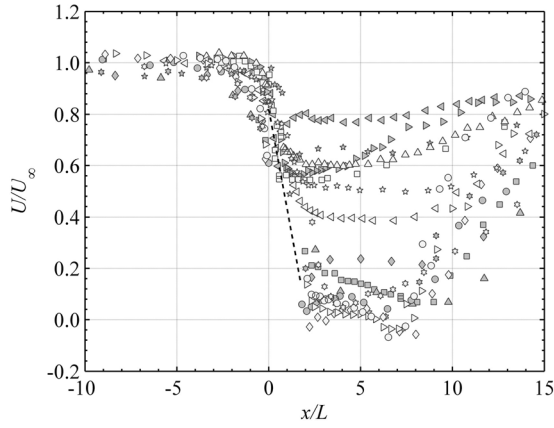
Figure 4. Longitudinal profiles of streamwise velocity. Velocity is normalized by upstream value, U_∞, and distance, x, is normalized by the adjustment length scale, L, defined in equation (1). The symbols are given in Table 1. The uncertainty in the mean velocity is 0.1 cm s^{-1}, corresponding to U/U_∞ on the order of 0.01, which is comparable to the symbol size.

upstream velocity, U_∞. Using the nondimensional deceleration defined in (2), the exit velocity U_e is

$$\frac{U_e}{U_\infty} = \frac{U_0}{U_\infty} - \frac{\partial(u/U_\infty)}{\partial(x/L)}\frac{D}{L} = \frac{U_0}{U_\infty} - A\frac{D}{L} \quad (3)$$

To estimate U_0, we assume the deceleration upstream of the patch has rate $A_0 \sim A$ over length scale $L_o \sim D$, and introduce the combined scale factor, α, i.e., $A_0 L_0 = \alpha A D$.

$$\frac{U_0}{U_\infty} = 1 - A_0\frac{L_0}{L} = 1 - \alpha A\frac{D}{L} \quad (4)$$

Combining (3) and (4),

$$\frac{U_e}{U_\infty} = 1 - A\alpha\frac{D}{L} - A\frac{D}{L} = 1 - A(\alpha+1)\frac{D}{L} = 1 - \beta\frac{D}{L} \quad (5)$$

The scale factor $\beta = A(\alpha + 1)$ is obtained by least squares fit to the measured exit velocities. With a 95% confidence interval, $\beta = 0.42 \pm 0.03$.
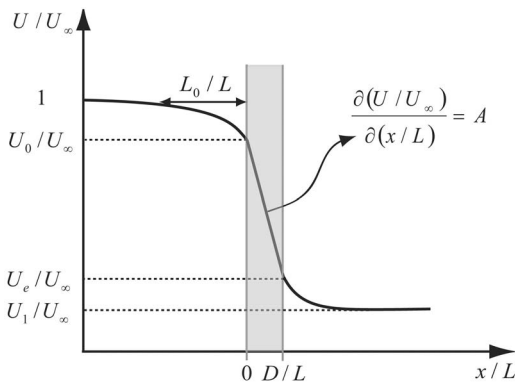

Figure 5. Schematic of velocity adjustment near a circular patch. Gray shading indicates position of patch between $x/L = 0$ and D/L. U_0, U_e, U_1 are velocities at the leading edge, at the trailing edge, and in the steady wake, respectively. L is the length scale of flow adjustment defined in equation (1). L_0 indicates the upstream flow adjustment distance.
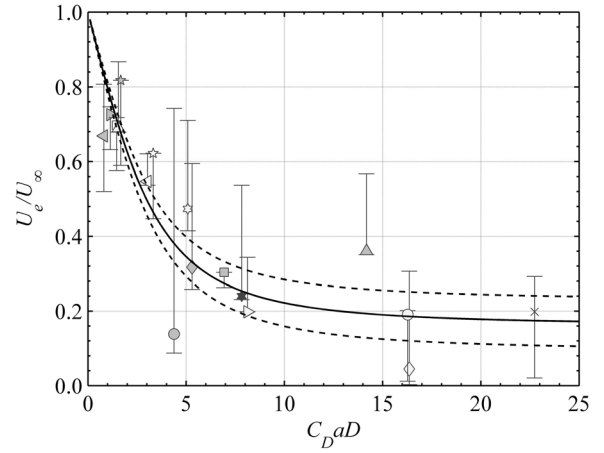

Figure 6. Variation of exit velocity, U_e, with flow blockage, $C_D a D$. Symbols are given in Table 1. Equation (5) is shown as a solid line and the 95% confidence intervals are shown as dashed lines. C_D is estimated from Figure 5 of *Tanino and Nepf* [2008], based on ϕ and the stem Reynolds number.

[15] Within measurement uncertainty, equation (5) describes the measured variation in U_e with flow blockage (Figure 6). For low-flow blockage ($C_D a D < 4$), U_e drops off quickly with increasing flow blockage. In this range, $L \approx 2(C_D a)^{-1}$, reducing (5) to the linear function, $U_e/U_\infty \approx 1 - 0.21\ C_D a D$. For high-flow blockage ($C_D a D > 4$), $L \approx D/2$ reducing (5) to $U_e/U_\infty \approx 0.16$. The presence of even this small value of U_e is sufficient to alter the von Karman vortex street, as we discuss below.

[16] Observations taken from previous studies validate the model proposed for U_e. First, *Takemura and Tanaka* [2007] considered groups of emergent, circular cylinders with six ratios of cylinder spacing to cylinder diameter corresponding to $a = 0.05, 0.11, 0.18, 0.36, 0.56,$ and 0.73 cm^{-1}. The corresponding patch diameters were $D = 13, 9, 7, 5, 4$ and 3.5 cm, respectively. The drag coefficients were calculated from data provided (1.4, 1.5, 1.5, 1.4, 1.7, and 2.1, respectively). Takemura and Tanaka measured velocity at seven points in a lateral transect located 1 cm downstream from the patch. The average of these points is used as an estimate of U_e. Their experiments use two configurations of cylinders, staggered and grid. The difference between these two configurations is used as a measure of the uncertainty in (5) associated with the specific arrangement of stems within a patch, which is not reflected in (5). That is, different configurations might produce the same aD, but different U_e. Second, *Ball et al.* [1996] considered a square array ($D \approx 42$ cm) of regularly spaced vertical piles. From spacing ratios given in their paper, we estimate $a = 0.04, 0.09,$ and 0.18 cm^{-1}. The velocity distribution at the downstream face of the model was measured by particle-tracking velocimetry technique, from which we estimate U_e. For Ball's study, C_D (1.2, 1.4, and 3, respectively) was estimated with the method described for our experiments. For all but two data points, the model prediction (5) agrees with the measurement within uncertainty (Figure 7).

3.2. Steady Wake Velocity (U_1) and Length Scale (L_1)

[17] Directly behind the patch the streamwise velocity decreases from U_e to the steady wake velocity U_1 within about one patch diameter (Figure 2). Velocity U_1 is maintained
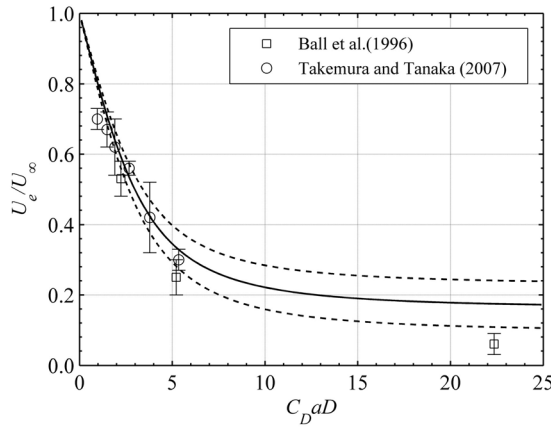
Figure 7. Model equation (5) (solid line) with 95% confidence limits (dashed lines). The model prediction is consistent with the measurements from *Ball et al.* [1996] and *Takemura and Tanaka* [2007].

until a distance L_1 from the back of the patch. Assuming that the slope of the normalized velocity after the patch is comparable to, or scales with, the slope through the patch, we expect that U_1 can be predicted from a form similar to (5). Fitting the measured U_1 in our experiment, we arrive at

$$\frac{U_1}{U_\infty} = 1 - (0.52 \pm 0.04)\frac{D}{L} \qquad (6)$$

For this fit, we excluded cases 4, 13, and 19, for which the wakes are approaching the solid body limit. These cases are discussed later. Equation (6) is shown as a solid black line in Figure 8a, with the 95% confidence limits shown by dashed lines. Recall that at the low-flow blockage limit, the adjustment length reduces to $L = 2(C_D a)^{-1}$, so that (6) may be simplified to

$$\frac{U_1}{U_\infty} \approx 1 - \frac{1}{4}C_D a D \qquad (7)$$

Note that this differs from the linear relation given by *Nepf* [2012b] because we use values of C_D estimated from previous measurements, whereas *Nepf* [2012b] assumed $C_D = 1$. For high-flow blockage, U_1 is negligibly small ($U_1/U_\infty \approx 0.03$), but not zero.

[18] The flow in the steady wake (U_1) separates two regions of faster velocity (U_2), creating a shear layer on either side of the steady wake (Figure 1). These layers grow linearly with distance from the patch, eventually meeting at the wake centerline, depicted by thin lines in Figure 1. When the shear layers meet, their interaction results in the von Karman vortex street. Thus, L_1 may be predicted from the growth of the linear shear layers. *Zong and Nepf* [2012] defined the distance from the edge of the patch to the inner edge of the shear layer as δ_1. Their observations confirmed that this length scale increases linearly with distance, as expected from previous studies of linear shear layer growth [e.g., *Dimotakis*, 1991]. With $\Delta U = U_2 - U_1$ and $\overline{U} = (U_1 + U_2)/2$, the growth of the shear layer is described by

$$\frac{d\delta_1}{dx} = S_1 \frac{\Delta U}{\overline{U}} \qquad (8)$$

S_1 is a constant (0.10 ± 0.02) across a wide range of D and ϕ values [*Zong and Nepf*, 2012]. The length scale L_1 extends from $x = D$ to a point at which $\delta_1 = D/2$. If we assume $\delta_1 = 0$ at $x = D$, $d\delta_1/dx = (D/2)/L_1$. Then, from (8) we can write

$$\frac{L_1}{D} = \frac{1}{2S_1}\frac{\overline{U}}{\Delta U} = \frac{1}{4S_1}\frac{(1 + U_1/U_2)}{(1 - U_1/U_2)} \approx \frac{1}{4S_1}\frac{(1 + U_1/U_\infty)}{(1 - U_1/U_\infty)} \qquad (9)$$

If the channel width is much greater than the patch diameter, we may assume that $U_2 \approx U_\infty$, resulting in the right-most term in (9). Using (6) to define U_1/U_∞, (9) can also be written

$$\frac{L_1}{D} \approx 2.5\frac{(4 - D/L)}{(D/L)} \qquad (10)$$

Equation (10) does a reasonable job of representing the observed variation in L_1 with $C_D a D$ (solid line in Figure 8b). The dashed lines in Figure 8b represent the uncertainty in the model due to the uncertainty in U_1/U_∞ obtained from (6).

[19] For low-flow blockage, we can use U_1/U_∞ defined in (7) instead of (6) to simplify (9). Specifically, for $C_D a D < 4$, we approximate

$$\frac{L_1}{D} = 2.5\left[\frac{8 - C_D a D}{C_D a D}\right] \quad \text{for} \ C_D a D < 4 \qquad (11)$$

For $C_D a D > 4$, we assume that $U_1 \approx 0$, for which (9) reduces to

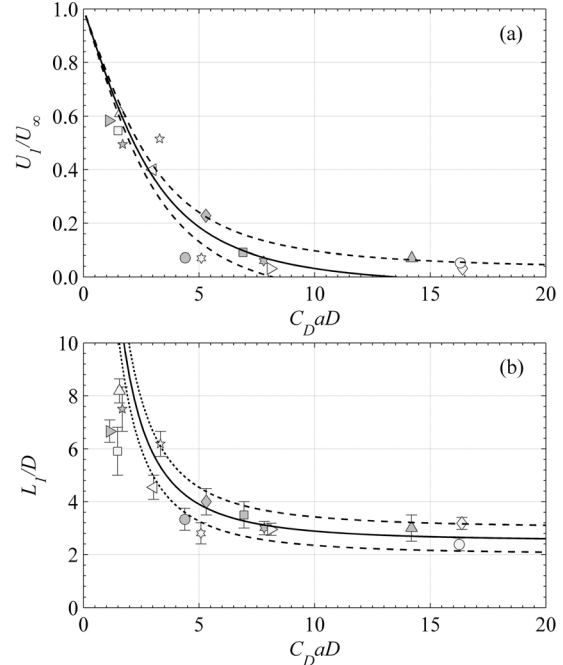$$L_1/D = 2.5 \quad \text{for} \ C_D a D > 4 \qquad (12)$$

Figure 8. Length and velocity scales of the steady wake. (a) Measured steady wake velocity, U_1, normalized by the upstream velocity, U_∞. Uncertainty is comparable to the symbol. Solid black line is equation (6), with 95% confidence limits shown by dashed lines. (b) Measured L_1. Solid line is prediction based on equation (10). C_D estimated from Figure 5 of *Tanino and Nepf* [2008], based on ϕ and the stem Reynolds number.
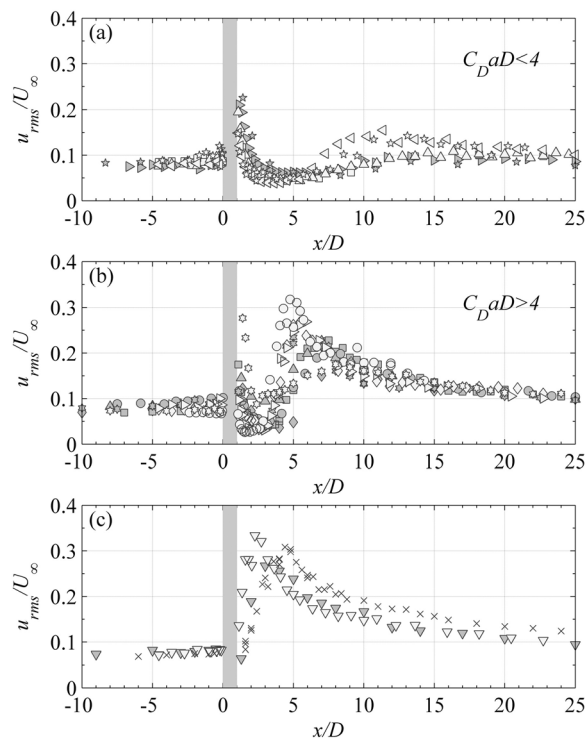
Figure 9. Longitudinal transect of turbulence intensity along the patch centerline. Gray region indicates patch position. (a) Low-flow blockage, $C_D aD < 4$; (b) high-flow blockage, $C_D aD > 4$; and (c) cases at solid body limit, $C_D aD = 23, 34,$ and 72, corresponding to cases 19, 4, and 13, respectively.

Note that even as the velocity behind the patch approaches zero, the delay in the von Karman vortex street persists, with $L_1/D = 2.5$. However, when $C_D aD$ becomes high enough that U_e becomes zero, the wake resembles that observed for a solid body, with a recirculation zone and vortex street forming directly behind the patch, so that $L_1 \approx 0$ (Figure 3, top). *Folkard* [2011] noted a similar transition in the wakes behind a submerged meadow of flexible blades that could change their posture in response to flow. Under higher flow conditions, the meadow was more compressed and effectively denser. For these conditions a recirculation zone formed in the wake of the patch. Under lower flow conditions, the meadow was less compressed, and effectively sparser, allowing flow to pass through the meadow, similar to the bleed flow discussed here. In these cases no recirculation was observed in the wake.

4. Turbulence in the Patch Wake

[20] Turbulence generated in the wake of a porous patch may impact sediment deposition and erosion. First, turbulent motions may dislodge individual sediment particles [e.g., *Diplas et al.*, 2008]. Second, elevated turbulence and the associated elevated vertical diffusivity may enhance the ability of a flow to keep sediment in suspension, facilitating sediment transport [*López and Garcia*, 1998]. For example, *Graf and Istiarto* [2002] showed that elevated turbulence intensity in the wake of a solid obstruction enhanced erosion and sediment transport. Here, we consider the turbulence in the wake of a porous obstruction, and in section 5 connect it to observed deposition.

[21] As discussed in section 1, the wake behind a porous obstruction may have two distinct regions of turbulence (Figure 1). The stem-scale turbulence generated by individual stems within the patch may be present in the patch and directly downstream. Patch-scale turbulence, i.e., the von Karman vortex street, is initiated at distance L_1 from the patch and reaches its peak intensity at L_w. These two sources give rise to two distinct peaks (u_{rms1} and u_{rms2} in Figure 1) in the longitudinal transect (Figure 9). While we use u_{rms} to characterize turbulence, the longitudinal distribution of TKE = $0.5(u_{rms}^2 + v_{rms}^2 + w_{rms}^2)$ follows the same trends.

[22] For a wake behind a solid obstruction, *Williamson* [1996] defined the wake formation length as the distance to the point of maximum u_{rms} associated with the von Karman vortex street. We borrow this concept to define the wake formation length L_w behind a porous patch as the distance to the second maximum of u_{rms}, which, as in the solid body definition, corresponds to the von Karman vortex street. Similar to the wake of a solid obstruction, a recirculation zone is present in the wakes of high-flow blockage patches ($C_D aD > 7.8$, Table 1). A recirculation zone is never observed behind a low-flow blockage patch ($C_D aD < 4$). The recirculation appears as a zone of negative velocity in the centerline transect (e.g., cases 4, 13, and 19 in Figure 3). When present, the recirculation zone occurs just before a peak in turbulence, i.e., similar to the solid body. A similar sequence of recirculation followed by a peak u_{rms} has also been observed behind porous plates [*Castro*, 1971].

[23] For low-flow blockage patches ($C_D aD < 4$) the first peak in turbulence is greater than the second (Figure 9a). As the flow blockage decreases, the second peak moves downstream and decreases in magnitude, indicating that the strength of the von Karman vortex street is declining [see also *Zong and Nepf*, 2012]. Between the two peaks there is a minimum in turbulence level that is lower than the turbulence level observed upstream in the undisturbed upstream flow.

[24] For the high-flow blockage patches ($C_D aD > 4$, Figure 9b), the peak directly behind the patch is smaller than the downstream peak, i.e., $u_{rms1} < u_{rms2}$. There is one exception, case 18 (six-point stars in Figures 9b and 10c), for which $u_{rms1} > u_{rms2}$. For this case, we estimate $C_D aD = 5.1$, which is close to the expected transition ($C_D aD = 4$), and we suspect this case should actually fall in the low-flow blockage regime, but is mislabeled due to uncertainty in estimating C_D for this very narrow patch ($D = 5$ cm).

[25] For the highest values of flow blockages ($C_D aD = 23,$ 34, 72, shown in Figure 3), the wake of the porous patch approaches that of a solid body. As shown in Figure 3, these cases do not exhibit a steady wake zone, and a recirculation is located directly behind the patch. Consistent with this, there is a single peak in turbulence intensity (Figure 9c). For the highest flow blockage (case 13, $C_D aD = 72$) this peak occurs at a distance $L_W/D = 1.2$ from the patch, which matches the value observed behind a solid cylinder. For example, for $D = 22$ cm and 42 cm, *Zong and Nepf* [2012] observed $L_w/D = 1.1$ and 1.3, respectively. Only for $C_D aD \leq 16$ do we observe a steady wake (L_1 in Table 1) and two distinct peaks in turbulence intensity (Figure 9). From this we infer that the transition to solid body wake behavior occurs between 16 and 23, or roughly $C_D aD = 20$. A similar transition in wake behavior was observed by *Nicolle and Eames* [2011], who numerically simulated flow past arrays of circular cylinders with solid volume fractions from 0.002 to
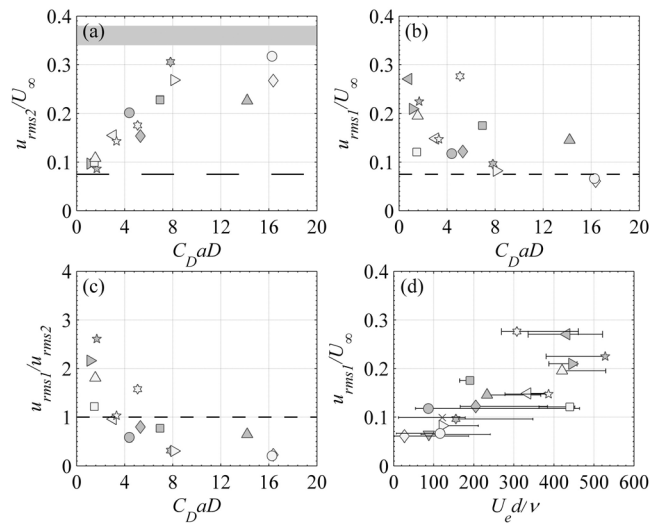
Figure 10. Turbulence intensity in the patch wake: (a) u_{rms2}/U_∞ (gray bar indicates value in wake of solid object), (b) u_{rms1}/U_∞, and (c) u_{rms1}/u_{rms2} versus C_DaD; and (d) u_{rms1}/U_∞ versus stem Reynolds number. Dashed line in Figures 10a and 10b indicates upstream turbulence intensity $u_{rms}/U_\infty = 0.075$. Case 5 is excluded in Figures 10a and 10c because no Karman vortex street is observed.

0.3. Based on Nicolle and Eames' Figure 10, the wake resembles that of a solid body for $\phi \geq 0.22$. For this case, $D/d = 21$ and $C_D = 4.6$ (based on stem Reynolds number $Re_d = 100$ and solid volume fraction $\phi = 0.22$), so that this transition corresponds to $C_DaD = (4/\pi)C_D \phi (D/d) = 27$, which is consistent with the transition inferred from our data set. Again note that here we use empirical estimates for C_D, which results is slightly different limits than discussed by *Nepf* [2012b], who assumed $C_D = 1$.

[26] The double peak in turbulence intensity has been observed behind other porous obstructions. *Lee and Kim* [1999] noted that the intensity of the second turbulence peak decreased as the fence porosity (ε) increased, and *Castro* [1971] made a similar observation behind thin perforated plates. A similar trend is observed in our data. However, because we consider different patch diameters, D, we can refine the parameterization to reflect D as well as ϕ. Note that porosity is simply $\varepsilon = 1 - \phi = 1 - (\pi/4)ad$. We observe that the intensity of the second peak increases as C_DaD increases, i.e., as either ϕ or D decrease (Figure 10a). In other words, for the same solid volume fraction (same porosity) a bigger patch can produce a larger turbulence intensity u_{rms2} (Table 1). For $C_DaD < 8$ the magnitude of u_{rms2} increases rapidly with C_DaD (Figure 10a). For higher flow blockage ($C_DaD > 8$), u_{rms2} is less sensitive to C_DaD, as the turbulence intensity approaches the limit for a solid obstruction (gray horizontal bar in Figure 10a). The three cases approaching the solid body limit (cases 4, 13, and 19, Figure 3), have turbulence ratios, $u_{rms2}/U_\infty = 0.28$, 0.33, and 0.31, respectively, compared to $u_{rms2}/U_\infty = 0.34$ and 0.38 observed for a solid body by *Zong and Nepf* [2012]. For solid obstructions, the von Karman vortex street is self-similar when velocities are scaled with the free-stream

velocity, U_∞, and distances are scaled by the obstruction diameter. We expect this to be valid for porous obstructions as well, such that the curves shown in Figures 9b and 10a are representative of any free stream velocity, as long as $U_\infty D/\nu > 100$, the criteria to form a von Karman vortex street [see also *Zong and Nepf*, 2012].

[27] The turbulence intensity in the first peak, u_{rms1}, is also a function of flow blockage (Figure 10b), decreasing as C_DaD increases. For high C_DaD, u_{rms1}/U_∞ approaches 0.075, which is the undisturbed upstream value (dashed line in Figure 10b). However, the turbulence is significantly higher than that expected from the local velocity, e.g., $u_{rms1}/U_e > 0.5$, which suggests that in the near wake the turbulence generated by individual stems is more important than that generated by local bed stress.

[28] As u_{rms2} and u_{rms1} have opposing tendencies with increasing C_DaD, the following transition occurs. For low-flow blockage ($C_DaD < 4$), $u_{rms1}/u_{rms2} > 1$ (Figure 10c), i.e., the turbulence is highest immediately downstream from the patch. However, for high-flow blockage, the turbulence intensity is highest at some distance removed from the patch. *Takemura and Tanaka* [2007] note a similar transition in wake turbulence. In their study, PKV and LKV correspond to stem-scale turbulence and patch-scale turbulence, respectively. First, patch-scale turbulence (LKV) was absent when the ratio of lateral cylinder spacing (G) to stem diameter (d) was greater than 2 [e.g., *Takemura and Tanaka*, 2007, Figure 13], which roughly corresponds to $C_DaD \leq 1.0$. Our case 5 ($C_DaD = 0.8$) fits into this regime, with only stem-scale turbulence observed in the wake. Second, *Takemura and Tanaka* [2007] also observed that when G/d drops below zero, which corresponds to $C_DaD \geq \approx 3$, the patch-scale turbulence becomes the dominant turbulent structures in the wake. This transition (recorded as $u_{rms1}/u_{rms2} < 1$) occurs for $C_DaD \geq 4$ in our study (Figure 10c). As discussed above, case 18 (six-point star) is an exception.

[29] The description of u_{rms1} is complicated by the fact that, unlike u_{rms2}, which exhibits similarity when scaled by U_∞, u_{rms1} is not directly related to U_∞, but rather is related to U_e. This means that the trends depicted in Figures 10b and 10c cannot be generalized to other values of U_∞. The intensity of turbulence generated by individual stem wakes is set by the stem-scale Reynolds number, $Re_d = U_ed/\nu$ (Figure 10d), with u_{rms1} increasing with increasing Re_d.

4.1. Wake Formation Length Scale, L_w

[30] For $C_DaD < 20$, the length scales L_1 and L_w are related, specifically $L_w/L_1 = [1.9 \pm 0.4]$, with L_w/L_1 decreasing slightly as C_DaD increases. Recall that L_1 is not defined at the solid body limit, $C_DaD > 20$. Since L_1 marks the beginning of the von Karman vortex street and L_w marks its peak intensity, the nearly constant ratio L_w/L_1 tells us that when the vortex street is delayed downstream (larger L_1), it also evolves more slowly. This is consistent with the observed strength of the von Karman vortices, reflected in u_{rms2}/U_∞. Specifically, as the vortex strength decreases, L_w/D increases (Figure 11). Previous studies of wake bleed flow indicate that L_w increases as the bleed flow U_e increases [e.g., *Wood*, 1967]. Since we established above that U_e is a function of C_DaD, we expect that L_w is also a function of C_DaD. Indeed, we find this is the case in Figure 11b. Further, as C_DaD approaches the limit of
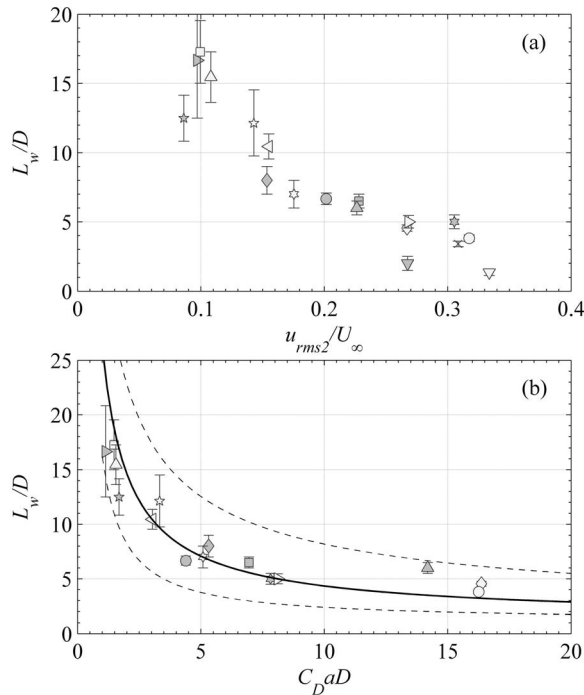
Figure 11. Wake formation length, L_w related to (a) u_{rms2}/U_∞, and (b) $C_D aD$. Solid and dashed lines represent mean and 95% confidence limit of empirical fit given in equation (13).

solid body wake behavior ($C_D aD > 20$), we expect $L_w/D \approx 1.2$. The following power law is consistent with this limit,

$$\frac{L_w}{D} = 1.2 + (25 \pm 10)C_D aD^{(-0.9\pm0.2)} \qquad (13)$$

Equation (13) is shown by a solid line in Figure 11b, with 95% confidence limits shown by dashed lines.

[31] *Folkard* [2005] observed a wake formation length behind a submerged seagrass model that agrees with the empirical fit given in (13). In his study, a peak in Reynolds stress occurred at $L_w = 115$ cm behind a meadow of height $h_v \approx 17$ cm [*Folkard*, 2005, Figure 6]. Geometrically, the patch centerline shown in Figure 1 is similar to the bed for a submerged meadow, so that $D = 2h_v$. Each stem in Folkard's meadow had six blades of width $d = 1$ cm and $n = 750$ stem m^{-2}, so that $a = 6nd$, $=0.45$ cm^{-1}, and the equivalent flow blockage is $C_D aD = 16$ (assuming $C_D = 1$). For this, (13) predicts $L_w/D = 3.3$, which is consistent with the observed value, $L_w/2h_m = 3.4$. Ecologically, it interesting to note that both patch configurations lead to a relatively quiescent region immediately downstream of the plant patch, which is likely to be a region in which the plants find it easier to grow (see discussion in section 5). This is an example of ecosystem engineering, organisms altering their physical habitat to the advantage of themselves or other organisms [*Jones et al.*, 1994].

5. Deposition Pattern Reflects the Wake Structure

[32] Patches of channel vegetation have been observed to grow predominantly in the downstream direction [*Sand-Jensen and Madsen*, 1992]. This expansion is linked, at least in part, to the deposition of fine material in the wake of

an existing patch, which provides ideal substrate for germination and establishment of seedlings [*Scott et al.*, 1996; *Gurnell et al.*, 2001; *Schnauder and Moggridge*, 2009]. The diminished velocity within the wake should promote deposition, relative to the free stream, and thus the length scale defining the region of depressed velocity (L_1) may predict the region of enhanced deposition. Further downstream, enhanced turbulence levels can inhibit deposition, so that the length scale L_w may predict a region of diminished deposition. To explore the connection between the deposition footprint and the length scales L_1 and L_w, we measured the deposition pattern for a high- and low-flow blockage patch: case 17 ($C_D aD = 16$, Figure 12) and case 16 ($C_D aD = 3.3$, Figure 13), respectively. In each figure the deposition measured in a control experiment (2.50 ± 0.05 mgcm^{-2}, SD of spatial variation) is shown by a horizontal gray bar.

[33] First consider deposition upstream of the patch. For the high-flow blockage patch (Figure 12) deposition is enhanced, relative to the control, in the region of flow deceleration upstream of the patch. *Gurnell et al.* [2001] and *Zong and Nepf* [2010] also observed enhanced deposition upstream of a patch and attributed it to diminished local bed stress, i.e., as the velocity and bed shear stress decrease in the streamwise direction, net deposition increases. The deceleration is less pronounced in the low-flow blockage case, and consistent with this there is no enhancement in deposition upstream of this patch (Figure 13).

[34] Second, in both cases (Figures 12 and 13) deposition is diminished within the patch, relative to the control. The explanation for this is clear for the sparse patch (Figure 13), for which velocity was measured within the patch. Although the mean velocity is reduced within the patch, the turbulence is elevated by up to a factor of three above the free stream. Although velocity was not measured within the dense patch (Figure 12), we can infer that the turbulence level was also elevated within this patch. The stem Reynolds number estimated from the exit velocity, $Re_d = U_e d/\nu = 115$, is a lower bound for Re_d within the patch, because the velocity within the patch is everywhere higher than U_e. $Re_d > 100$ indicates that stem-scale turbulence was likely generated within this patch, and probably inhibited deposition. Similarly, *Zong and Nepf* [2010] observed a region of diminished net deposition within the leading edge of a long patch, and they attributed this to the elevated levels of turbulence measured in that region. *Neumeier* [2007] observed elevated turbulence within the leading edge of a marsh grass, *Spartina anglica*, and suggested that the elevated turbulence may reduce sedimentation at the vegetation edge. In our study, because the patch is finite in length, the entire patch experiences elevated turbulence and diminished deposition. However, *Takemura and Tanaka* [2007] note that when the cylinder-to-cylinder spacing becomes too small ($G/d <$ zero in a staggered array, corresponding to $\phi > 0.44$), cylinder-generated turbulence may be suppressed.

[35] Our observation of diminished deposition within the circular patch stands in contrast to other previous studies that have observed enhanced deposition inside vegetated regions [e.g., *Cotton et al.*, 2006; *Gurnell et al.*, 2006]. *Cotton et al.* [2006] note that processes other than flow dynamics may control the capture of suspended particles in macrophyte beds. For example, suspension feeders living within the vegetated region ingest particulate organic matter and produce fecal pellets, which, being much larger in size
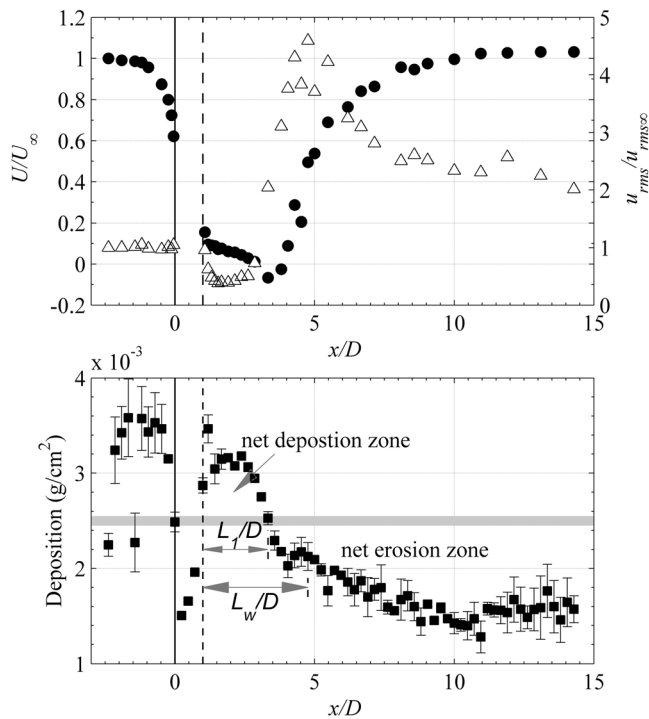
Figure 12. (top) Velocity (solid circle) on left-hand axis, u_{rms} (triangle) on right-hand axis, and (bottom) deposition along patch centerline for the high-flow blockage case 17 ($D = 42$ cm, $C_D aD = 16$). The patch exists between $x/D = 0$ (solid vertical line) and 1 (dashed vertical line). Horizontal gray bar in Figure 12 (bottom) denotes the deposition in control experiment, and its vertical width reflects the standard deviation of measurement.

than the original suspended material, can more easily settle within the vegetation. Suspended material may also settle onto plant surfaces [*Palmer et al.*, 2004] or be filtered out between closely spaced leaves [*Cotton et al.*, 2006].

[36] Finally, we consider the deposition in the wake of the patch. For the dense patch (Figure 12), net deposition is enhanced behind the patch, but diminished further downstream. The sparse patch has a similar pattern (Figure 13), except for a thin region directly behind the patch, in which stem turbulence persists and inhibits deposition, an extension of the conditions within the patch. In this case, the deposition does not increase above the control until $x/D = 1.5$ (Figure 13). In both cases, however, the region of enhanced deposition extends to the end of the steady wake, L_1, corresponding to the region in which both the mean and turbulent velocities are diminished, relative to the open channel. The elevated turbulence associated with the Karman vortices, beginning near $x = L_w$, diminishes net deposition relative to the control. The reduction in net deposition is greater for the dense patch (Figure 12), which produced stronger Karman vortices, as suggested by the higher level of turbulence at and beyond $x = L_w$ (compare Figures 12, top, and 13, top). Similarly, *Tsujimoto* [1999] observed deposition of fine material behind a dense patch of model vegetation. The deposition formed a triangular region that extended a distance of about $2.5D$ downstream from the back of the patch [*Tsujimoto*, 1999, Photo 3]. This length scale is consistent with the value L_1/D observed for dense patches (Figure 8).

[37] *Tanaka and Yagisawa* [2010] investigated sedimentation near vegetation in the field, where a range of sediment sizes was present. When the vegetation density was high (spacing/diameter = $G/d < 0.5$), such as with willow (*Salix subfragilis*), deposition in the wake was of significantly finer grain material (0.1 to 1 mm) than that within and upstream of the patch (10 to 100 mm). This stem spacing corresponds to $\phi > \approx 0.14$ (based on data given by *Takemura and Tanaka* [2007]). When the vegetation density was low (spacing/diameter = $G/d > 1$, $\phi < \approx 0.09$), such as *Robinia pseudoacacia*, the deposition in the wake consisted of only slightly finer material, but falling in the same size range (10 to 100 mm) as that deposited within and upstream of the patch. These observations suggest that when a range of particle sizes are available, a denser patch produces a greater degree of particle size segregation, probably because the denser patch creates a wake with flow conditions of greater distinction from the free stream, in both mean and turbulent measures (compare Figures 12, top, and 13, top). This important detail is not evident within our deposition data because we considered a single particle size.

[38] Based on Figures 12 and 13 and the discussion above, we conjecture that the presence of the von Karman vortex street, and its associated high levels of turbulence, sets the maximum length scale of enhanced deposition behind the patch, and potentially the maximum streamwise extension of the patch. As the patch grows into the downstream region of enhanced deposition, the patch geometry becomes more
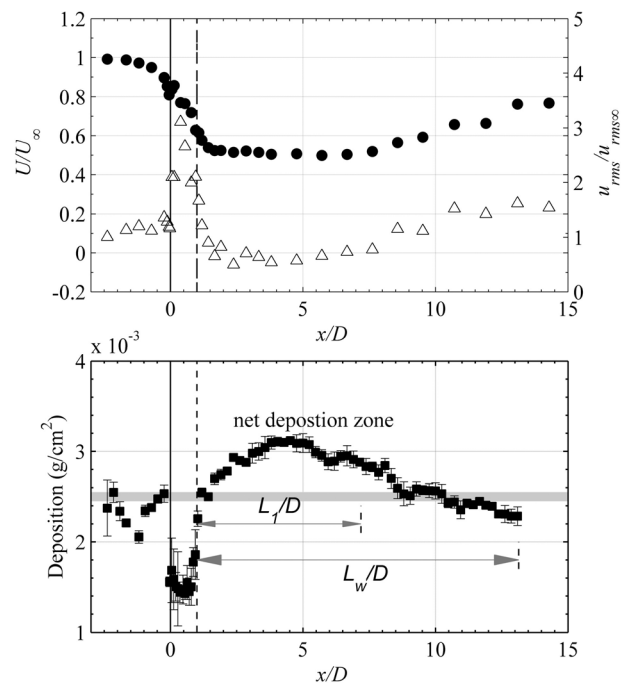

Figure 13. (top) Velocity (solid circle) on left-hand axis, u_{rms} (triangle) on right-hand axis, and (bottom) deposition along patch centerline for low-blockage case 16 ($D = 42$ cm, $C_D aD = 3.3$). The patch exists between $x/D = 0$ (solid vertical line) and 1 (dashed vertical line). Horizontal gray bar in Figure 13 (bottom) denotes the deposition in control experiment, and its vertical width reflects the standard deviation of measurement.

streamline. We propose that at some point the patch becomes sufficiently streamlined that it no longer produces a wake of diminished velocity. At this point, the patch no longer promotes deposition downstream of its trailing edge, and the patch will no longer lengthen in the streamwise direction. Observations of patch geometry in the field suggest that a stable geometry exists for ratios of patch length to patch width of 2.5 [*Sand-Jensen and Madsen*, 1992]. A similar aspect ratio has been suggested for in-stream plant islands [*Schnauder and Moggridge*, 2009]. Future work is underway to test this hypothesis.

6. Conclusions

[39] Using 19 combinations of patch diameter, D, and patch density, a, we have shown that the adjustment of flow to a circular patch of emergent vegetation can be described by the spatial scale factor, L, which is the greater of the following two patch length scales: the patch half width, $D/2$, and the drag length scale $L_c = 2(1 - \phi)/C_D a$. Using this scale factor, we developed a model that predicts the velocity exiting a porous patch. The model was validated with data from two other studies, with different patch configurations. The following regimes were identified. For low-flow blockage ($C_D a D < 4$), L is reduced to $\approx 2(C_D a)^{-1}$, and $U_e/U_\infty \approx 1 - 0.2 C_D a D$. For high-flow blockage ($C_D a D > 4$), $L \approx D/2$, reducing (5) to $U_e/U_\infty \approx 0.16$. Similar relationships were developed for the steady wake velocity, U_1. The presence of even a low value of U_e is sufficient to delay the onset of the von Karman vortex street, creating a steady wake region in which both velocity and turbulence remain diminished, relative to the free stream. For the highest flow blockages ($C_D a D > 20$), the wake structure is similar to that of a solid body.

[40] The turbulence in the wake has two peaks. The first peak is located directly behind the patch and reflects stem-scale turbulence generated by individual stems within the patch. The second peak is located at a distance L_w behind the patch and reflects the patch-scale turbulence associated with the von Karman vortex street. As flow blockage increases, the first peak decreases and the second peak both increases and shifts its position closer to the patch, i.e., L_w decreases. For $C_D a D > 20$, the position and magnitude of the second peak approaches that produced by solid body. Within the steady wake, where both the mean velocity and turbulence levels are low, net deposition is enhanced, relative to the open channel control. The region of enhanced deposition can be predicted from the wake length scale, L_1, which is a function of flow blockage. Within the far wake, i.e., beyond L_w, high levels of turbulence associated with the von Karman vortex street inhibit deposition.

References

Ball, B. J., P. K. Stansby, and N. Alliston (1996), Modeling shallow water flow around pile groups, *Proc. Inst. Civ. Eng. Water Marit. Energy*, *118*, 226–236, doi:10.1680/iwtme.1996.28987.

Belcher, S. E., N. Jerram, and J. C. R. Hunt (2003), Adjustment of a turbulent boundary layer to a canopy of roughness elements, *J. Fluid Mech.*, *488*, 369–398, doi:10.1017/S0022112003005019.

Bennett, S., W. Wu, C. V. Alonso, and S. Y. Wang (2008), Modeling fluvial response to in-stream woody vegetation: Implications for stream corridor restoration, *Earth Surf. Processes Landforms*, *33*, 890–909, doi:10.1002/esp.1581.

Bouma, T. J., M. Friedrichs, B. K. van Wesenbeeck, S. Temmerman, G. Graf, and P. M. J. Herman (2009), Density-dependent linkage of scale-dependent feedbacks: A flume study on the intertidal macrophyte *Spartina anglica*, *Oikos*, *118*, 260–268, doi:10.1111/j.1600-0706.2008.16892.x.

Castro, I. P. (1971), Wake characteristics of two-dimensional perforated plates normal to an air-stream, *J. Fluid Mech.*, *46*, 599–609, doi:10.1017/S0022112071000727.

Chen, D., and G. Jirka (1995), Experimental study of plane turbulent wakes in a shallow water layer, *Fluid Dyn. Res.*, *16*, 11–41, doi:10.1016/0169-5983(95)00053-G.

Cotton, J., G. Wharton, J. Bass, C. Heppell, and R. Wotton (2006), The effects of seasonal changes to in-stream vegetation cover on patterns of flow and accumulation of sediment, *Geomorphology*, *77*, 320–334, doi:10.1016/j.geomorph.2006.01.010.

Dimotakis, P. E. (1991), Turbulent free shear layer mixing and combustion, in *High-Speed Flight Propulsion Systems*, edited by S. N. B. Murthy and E. T. Curran, pp. 265–340, Am. Inst. of Aeron. and Astron., Washington, D. C.

Diplas, P., C. Dancy, A. Celik, M. Valyrakis, K. Greer, and T. Akar (2008), The role of impulse on the initiation of particle movement under turbulent flow conditions, *Science*, *322*, 717–720, doi:10.1126/science.1158954.

Folkard, A. (2005), Hydrodynamics of model *Posidonia oceanica* patches in shallow water, *Limnol. Oceanogr.*, *50*(5), 1592–1600, doi:10.4319/lo.2005.50.5.1592.

Folkard, A. (2011), Flow regimes in gaps within stands of flexible vegetation: Laboratory flume simulations, *Environ. Fluid Mech.*, *11*(3), 289–306, doi:10.1007/s10652-010-9197-5.

Fonseca, M. S., J. C. Zieman, and G. W. Thayer (1983), The role of current velocity in structuring eelgrass (*Zostera marina L.*) meadows, *Estuarine Coastal Shelf Sci.*, *17*(4), 367–380, doi:10.1016/0272-7714(83)90123-3.

Gedan, K. B., M. L. Kirwan, E. Wolanski, E. B. Barbier, and B. R. Silliman (2011), The present and future role of coastal wetland vegetation in protecting shorelines: Answering recent challenges to the paradigm, *Clim. Change*, *106*, 7–29, doi:10.1007/s10584-010-0003-7.

Graf, W. H., and I. Istiarto (2002), Flow pattern in the scour hole around a cylinder, *J. Hydraul. Res.*, *40*(1), 13–20, doi:10.1080/00221680209499869.

Gurnell, A. M., G. E. Petts, D. M. Hannah, B. P. G. Smith, P. J. Edwards, J. Kollmann, J. V. Ward, and K. Tockner (2001), Riparian vegetation and island formation along the gravel-bed Fiume Tagliamento, Italy, *Earth Surf. Processes Landforms*, *26*, 31–62, doi:10.1002/1096-9837(200101)26:1<31::AID-ESP155>3.0.CO;2-Y.

Gurnell, A., M. van Oosterhout, B. de Vlieger, and J. M. Goodson (2006), Reach-scale interactions between aquatic plants and physical habitat: River Frome, *River Res. Appl.*, *22*(6), 667–680, doi:10.1002/rra.929.

Jones, C., J. H. Lawton, and M. Shachak (1994), Organisms as ecosystems engineers, *Oikos*, *69*, 373–386, doi:10.2307/3545850.

Kemp, J. L., D. M. Harper, and G. A. Crosa (2000), The habitat-scale ecohydraulics of rivers, *Ecol. Eng.*, *16*(1), 17–29, doi:10.1016/S0925-8574(00)00073-2.

Lee, S. J., and H. B. Kim (1999), Laboratory measurements of velocity and turbulence field behind porous fences, *J. Wind Eng. Ind. Aerodyn.*, *80*, 311–326, doi:10.1016/S0167-6105(98)00193-7.

López, F., and M. Garcia (1998), Open-channel flow through simulated vegetation: Suspended sediment transport modeling, *Water Resour. Res.*, *34*(9), 2341–2352, doi:10.1029/98WR01922.

Micheli, E. R., and J. W. Kirchner (2002), Effects of wet meadow riparian vegetation on streambank erosion. 2. Measurements of vegetated bank strength and consequences for failure mechanics, *Earth Surf. Processes Landforms*, *27*, 687–697, doi:10.1002/esp.340.

Nepf, H. M. (2012a), Flow and transport in regions with aquatic vegetation, *Annu. Rev. Fluid Mech.*, *44*, 123–142, doi:10.1146/annurev-fluid-120710-101048.

Nepf, H. M. (2012b), Hydrodynamics of vegetated channels, *J. Hydraul. Res.*, *50*(3), 262–279, doi:10.1080/00221686.2012.696559.

Neumeier, U. (2007), Velocity and turbulence variations at the edge of salt-marshes, *Cont. Shelf Res.*, *27*, 1046–1059, doi:10.1016/j.csr.2005.07.009.

Nicolle, A., and I. Eames (2011), Numerical study of flow through and around a circular array of cylinders, *J. Fluid Mech.*, *679*, 1–31, doi:10.1017/jfm.2011.77.

Palmer, M., H. Nepf, T. Pettersson, and J. Ackerman (2004), Observations of particle capture on a cylindrical collector: Implications for particle accumulation and removal in aquatic systems, *Limnol. Oceanogr.*, *49*, 76–85, doi:10.4319/lo.2004.49.1.0076.

Rominger, J., and H. M. Nepf (2011), Flow adjustment and interior flow associated with a rectangular porous obstruction, *J. Fluid Mech.*, *680*, 636–659, doi:10.1017/jfm.2011.199.

Sand-Jensen, K., and T. V. Madsen (1992), Patch dynamics of the stream macrophyte, *Callitriche cophocarpa*, *Freshwater Biol.*, *27*, 277–282, doi:10.1111/j.1365-2427.1992.tb00539.x.

Schnauder, I., and H. Moggridge (2009), Vegetation and hydraulic-morphological interactions at the individual plant, patch and channel scale, *Aquat. Sci.*, *71*, 318–330, doi:10.1007/s00027-009-9202-6.

Schulz, M., H. Kozerski, T. Pluntke, and K. Rinke (2003), The influence of macrophytes on sedimentation and nutrient retention in the lower River Spree (Germany), *Water Res.*, *37*(3), 569–578, doi:10.1016/S0043-1354(02)00276-2.

Scott, M., J. Friedman, and G. Auble (1996), Fluvial process and the establishment of bottomland trees, *Geomorphology*, *14*, 327–339, doi:10.1016/0169-555X(95)00046-8.

Takemura, T., and N. Tanaka (2007), Flow structures and drag characteristics of a colony-type emergent roughness model mounted on a flat plate in uniform flow, *Fluid Dyn. Res.*, *39*, 694–710, doi:10.1016/j.fluiddyn.2007.06.001.

Tanaka, N., and J. Yagisawa (2010), Flow structures and sedimentation characteristics around clump-type vegetation, *J. Hydro-environ. Res.*, *4*(1), 15–25, doi:10.1016/j.jher.2009.11.002.

Tanino, Y., and H. Nepf (2008), Laboratory investigation of mean drag in a random array of rigid, emergent cylinders, *J. Hydraul. Eng.*, *134*(1), 34–41, doi:10.1061/(ASCE)0733-9429(2008)134:1(34).

Temmerman, S., T. J. Bouma, J. Van de Koppel, D. van der Wal, M. B. de Vries, and P. M. J. Herman (2007), Vegetation causes channel erosion in a tidal landscape, *Geology*, *35*(7), 631–634, doi:10.1130/G23502A.1.

Tsujimoto, T. (1999), Fluvial processes in streams with vegetation, *J. Hydraul. Res.*, *37*(6), 789–803, doi:10.1080/00221689909498512.

Vandenbruwaene, W., et al. (2011), Flow interaction with dynamic vegetation patches: Implications for biogeomorphic evolution of a tidal landscape, *J. Geophys. Res.*, *116*, F01008, doi:10.1029/2010JF001788.

White, B., and H. Nepf (2007), Shear instability and coherent structures in shallow flow adjacent to a porous layer, *J. Fluid Mech.*, *593*, 1–32, doi:10.1017/S0022112007008415.

Wilcock, R., P. Champion, J. Nagels, and G. Crocker (1999), The influence of aquatic macrophytes on the hydraulic and physico-chemical properties of a New Zealand lowland stream, *Hydrobiologia*, *416*, 203–214, doi:10.1023/A:1003837231848.

Williamson, C. H. K. (1996), Vortex dynamics in the cylinder wake, *Annu. Rev. Fluid Mech.*, *28*, 477–539, doi:10.1146/annurev.fl.28.010196.002401.

Wood, C. J. (1967), Visualization of an incompressible wake with base bleed, *J. Fluid Mech.*, *29*, 259–272, doi:10.1017/S0022112067000795.

Zong, L., and H. Nepf (2010), Flow and deposition in and around a finite patch of vegetation, *Geomorphology*, *116*, 363–372, doi:10.1016/j.geomorph.2009.11.020.

Zong, L., and H. Nepf (2012), Vortex development behind a finite porous obstruction in a channel, *J. Fluid Mech.*, *691*, 368–391, doi:10.1017/jfm.2011.479.